



Nullclines entanglement induced topological transitions in driven liquid crystal cells

Marcel G. Clerc, R. Gajardo-Pizarro*

Departamento de Física and Millennium Institute for Research in Optics, FCFM, Universidad de Chile, Casilla 487-3, Santiago, Chile

ARTICLE INFO

Keywords:

Defects
Topological transitions
Vortices
Self-organisation

ABSTRACT

Physical systems can exhibit transitions between states with and without topological properties. These transitions have been observed in conductors to superconductors, fluids to superfluids, chiral magnets, and liquid crystal phases. Likewise, topological transitions have been observed by driving homogeneous liquid crystal cells. However, the mechanism of the formation of topological lattices has not been established. Here, we reveal an out-of-equilibrium topological transition mechanism. A vortex triplet is trapped in a nematic liquid crystal layer by the combined action of a magnetic ring and an oscillating electric field. By lowering the frequency, we observed that the nullcline curves of the vortex touch each other, creating new vortices. This nullcline entanglement process generates the emergence of a vortex lattice. Theoretically, based on a phenomenological amplitude equation valid close to the reorientation instability with the phenomenological inclusion of inertial effects, we observe a trapped vortex, oscillations, and entanglement of its nullcline curves, which generate new vortices and lattices in agreement with experimental findings.

1. Introduction

States of matter such as Bose–Einstein condensates [1], superfluidity [2], superconductivity [3], chiral magnets [4], and liquid crystalline blue phases [5] are topological or exotic states of matter rather than an aggregation of matter such as solid, liquid, gas, and plasma states. By modifying their physical parameters, these systems present surprising physical properties such as superconductivity due to topological transitions (Cooper pairs). These transitions of the matter were initially proposed by Berezinskii [6] and Kosterlitz and Thouless [7], who showed that a two-dimensional system described by a physical vector order parameter in thermodynamic equilibrium undergoes a transition from a homogeneous state to a state where vorticity persists when temperature decreases. The homogeneous state is characterised by all the vectors being aligned in the same direction to minimise the free energy. In opposition, thermal fluctuations may be responsible for creating different orientation domains connected through vortices or phase singularities [8]. Indeed, the topological transition is a balance between the interaction of vortices that minimise free energy and thermal fluctuations. Phase singularity corresponds to a point in space where the orientation of the vector field is not well defined. These vortices or phase singularities are an everyday phenomenon in fluids, corresponding to the centre of eddies. The winding number, *topological charge*, is introduced to characterise the physical vector field around a vortex [8]. This integer number represents the total number of times

the vector field winds around the singularity while varying along a closed, counterclockwise-oriented curve around the singular point. The total winding number of the system is conserved due to the topological stability of the system [8]. Hence, vortices are created or annihilated by pairs of opposite topological charges.

Nematic liquid crystal cells are a natural playground for studying vortices [5,9]. As a result of the orientational but not positional order of the rod molecules that make up the nematic liquid crystal phase, this type of soft matter is described by a direction vector $\vec{n}(\vec{r}, t)$ and a scalar order parameter $S(\vec{r}, t)$. In the case of liquid crystal cells with homeotropic anchoring, i.e. the molecules are oriented orthogonally to the wall cells, and the application of electric or magnetic fields induces disclination lines or vortices for the director. These vortices are usually called umbilical defects [10] or disclination lines [5,9] in the liquid crystals context. The umbilical defects are three-dimensional defect lines, such as a vertical string, in a thin cell in the vertical direction. In the case of thin cells with a thickness of less than a hundred microns, as a consequence of the confinement, the defects behave as quasi-2D defects; namely, they do not twist or deform in the vertical direction. These defects account for the rotation of the director vector \vec{n} averaged in the vertical direction of the cell, presenting phase singularities at their core. The charge is positive or negative, *the winding number*, when the director around the defect rotates clockwise or counterclockwise

* Corresponding author.

E-mail address: roberto.gajardo.p@ug.uchile.cl (R. Gajardo-Pizarro).

2π . Then, umbilical defects are created or annihilated by pairs of opposite charges [5,9]. To minimise the Frank–Oseen free energy of the system, umbilical defects of opposite sign (equal) charges attract (repel) between them [11]. The umbilical defects correspond to the different orientations of the directors with respect to their positions [5,9]. On the other hand, the refractive index of the cell depends on the director's average orientation. So, let us assume that the liquid crystal sample is considered between polarisers when they are oriented in parallel. In this case, dark lines (brush lines) corresponding to a direction projected onto the plane of the given director cell can be identified [5,9]. If the polarisers are crossed, two orthogonal director orientations can be identified, and the intersection of two of these curves identifies the position of the umbilical defects.

Experimental Berezinskii–Kosterlitz–Thouless thermal phase transitions in liquid crystal cells have not been observed because: (i) in thermodynamic equilibrium and homogeneous media, the vortices tend to annihilate in pairs to minimise the free energy, and (ii) liquid crystals are only observed over a narrow temperature range. The orientational order is lost at high temperatures, resulting in isotropic liquids. Likewise, the liquid crystal molecules crystallise at low temperatures, leaving a liquid crystal state. The above dynamics can be modified by incorporating inhomogeneities that can attract and trap umbilical defects, creating topological lattices [12–16]. Topological transitions have been observed by driving homogeneous liquid crystal cells out of equilibrium, e.g., by applying thermal gradients [17] or low-frequency electric fields [18,19]. Depending on the voltage and frequency, it is observed that the topological transitions are continuous or discontinuous, which presents different self-organisations of vortices. The origin and mechanism of the out-of-equilibrium topological transition and the creation of lattices is an open problem.

This work aims to understand and characterise the origin and mechanism of the topological transition-induced by an oscillatory electric field on a nematic liquid crystal cell. Based on the combined action of a magnetic ring and an oscillating electric field in a nematic liquid crystal layer, a vortex is trapped (see Fig. 1) [19]. The vortices are detected by observing the liquid crystal cell between two crossed polarisers, where the vortices correspond to the intersection of two black curves (black brushes). These black brushes correspond to the vertically average horizontal projection of the director being oriented parallel to one of the polarisers, which we coin as *nullcline curves*. The dynamics and interaction of vortices can be identified by observing their respective nullclines. By decreasing the frequency, it was observed that the nullclines of the vortex rotate around the vortex position [20]. We observe that at a critical frequency and voltage value, the nullclines touch each other, generating new vortices. This nullcline entanglement process generates the emergence of a vortex lattice, which is a non-equilibrium oscillatory state of the system (cf. Figs. 1b and 1c). Experimentally, we have characterised the phase space where we observe this topological transition (see Fig. 2). This transition is of a supercritical nature; that is, the number of vortices increases continuously as we decrease the voltage frequency. Theoretically, we observe a trapped vortex with oscillatory nullclines based on a phenomenological amplitude equation, which is valid close to the reorientation instability and includes phenomenologically inertial effects. In this model, as the frequency decreases, the nullcline curves entanglement generates new vortices and lattices of them (cf. Figs. 3 and 5). As a function of frequency, we observe that the transition is supercritical and gives rise to square lattices of vortices, which agrees with experimental findings.

2. Description of experimental setup

To investigate nullclines entanglement and topological transitions in driven liquid crystal cells, we consider a magnetic trap composed of a nematic liquid crystal cell (NLCC) under the influence of an oscillatory electric field and a magnetic ring [19]. Fig. 1a shows a schematic representation of the experimental setup. We consider a cell composed

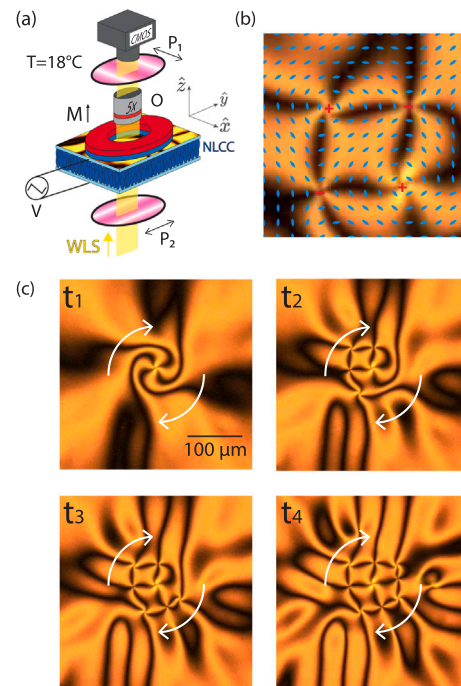


Fig. 1. Nullclines entanglement of a nematic liquid crystal vortex. (a) Schematic representation of the experimental setup. Nematic liquid crystal cell (NLCC) is under the effect of a magnet ring (M) and an oscillatory electric field generated by a triangle-shape voltage $V = V(V_0, \omega; t)$, where V_0 and ω are the intensity and frequency of the applied voltage. P_1 and P_2 are crossed and linear polarisers. The sample is illuminated by a white light source (WLS). O is an objective, and CMOS is a camera to monitor the liquid crystal cell. The blue rods account for a schematic representation of the average molecular orientation. (b) Snapshot of umbilical defects and its schematic representation of the vertical average of the director horizontal projection (blue rods) in the NLCC. Positive and negative symbols represent the position of positive and negative vortices, respectively. The positive and negative vortices exhibit a circular and hyperbolic organisation of rods around their phase singularity. (c) Time sequence of snapshots of a positive umbilical defect in a nematic liquid crystal cell ($V_0 = 10 V_{pp}$ and $\omega = 10$ mHz) generating a lattice by nullcline (black brush lines) entanglement ($t_1 = 0$ s, $t_2 = 200$ s, $t_3 = 300$ s, $t_4 = 500$ s). The intersection of four black brush lines accounts for a vortex. (For interpretation of the references to colour in this figure legend, the reader is referred to the web version of this article.)

of two thin glass layers with transparent electrodes included (indium tin oxide with a thickness of $0.08 \mu\text{m}$) and separated by a thickness of $d = 75 \mu\text{m}$, which are treated so that their inner walls have homogeneous homeotropic anchoring. By capillarity, the cell is filled with a nematic liquid crystal LC-BYVA-01 (INSTEC) with negative dielectric anisotropy $\epsilon_a = -4.89 \text{ Fm}^{-1}$, birefringence $\Delta n = n_e - n_o = 0.1$, rotation viscosity $\gamma = 204 \text{ mPa s}$, splay and bend elastic constants $K_1 = 17.65 \text{ pN}$ and $K_3 = 21.39 \text{ pN}$, respectively, and negative magnetic anisotropy χ_a (not measured yet). A neodymium magnetic ring of 3200 G on the surface with a rectangular cross-section, outer radius $R_{\text{out}} = 7 \text{ mm}$, inner radius $R_{\text{in}} = 2 \text{ mm}$, and thickness $h = 5 \text{ mm}$ is placed on the top of NLCC. The sample is placed in the microscope (Olympus BX51), sandwiched between two crossed linear polarisers and illuminated with a white light (halogen lamp), and a complementary metal–oxide–semiconductor (CMOS) camera (Thorlabs DCC1645C) monitors the liquid crystal cell's temporal evolution, allowing us to observe the central zone of the magnetic ring. The light intensity measured I_{BW} can be associated with the average molecular orientation of the nematic liquid crystal. A triangular voltage $V(t)$ of frequency ω and intensity V_0 is applied to the NLCC, where V_0 is above the critical reorientation voltage, *Fréedericksz voltage* [21], $V_{FT} = 6.57 V_{pp}$, ranging between 8 and $20 V_{pp}$. All experimental studies were conducted at room temperature ($T = 18 \text{ }^\circ\text{C}$).

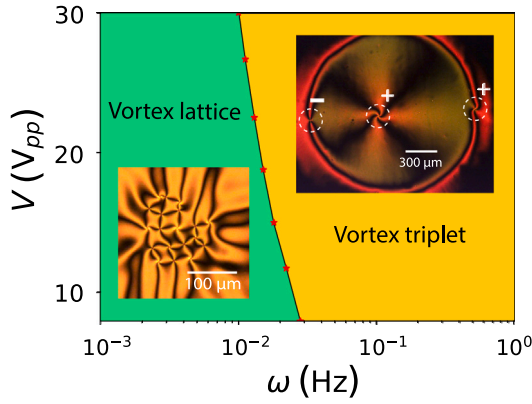


Fig. 2. Vortex phase diagram as a function of the frequency ω and intensity V_0 of the voltage. In the yellow region, a vortex triplet with and without electroconvection backgrounds is observed. In the green region, vortex lattices emerge as a topological transition. $\omega_{TT}(V_0)$ curve accounts for the critical frequency at which the supercritical topological transition occurs. Insets inside show the typical snapshots of the observed phenomena. The left and right panels show a vortex lattice and a vortex triplet, respectively. The dashed circles account for the vortices and the symbols + and – their corresponding charges. The stars account for the experimental results, and the lines that connect them have been interpolated to separate the two regions. (For interpretation of the references to colour in this figure legend, the reader is referred to the web version of this article.)

3. Experimental observation of nullclines entanglement and topological transitions

To generate a vortex and transition to a vortex lattice, we engender a vortex triplet using a magnetic trap composed of a nematic liquid crystal cell (NLCC) under the influence of an oscillatory electric field and a magnetic ring [19]. Fig. 1a shows a schematic representation of the experimental setup. By applying a triangular voltage, $V_0 > V_{FT}$, with a frequency ω of the order of one hertz in the nematic liquid crystal cell, we observe the emergence of several vortices. Subsequently, these are cancelled by pairs of opposite charges, ultimately giving rise to a triplet of stable vortices (cf. right bottom inset of Fig. 2). Considering the frequency ω as a control parameter, when the frequency is decreased, the nullcline of the central vortex begins to oscillate, *dancing vortices* [20]. By further decreasing the frequency from a critical frequency ω_{TT} , the nullcline curves of the central vortex begin to touch, generating new vortices and the emergence of a vortex lattice. Figs. 3a and 3b show, respectively, an experimental and numerical temporal sequence of the entanglement of the vortex nullclines and the generation of new vortices (see video 1 on the Supplementary Materials [22]). Therefore, as the nullclines become entanglement, the vortex lattice emerges until the system exhibits a non-equilibrium oscillatory state in which the number of vortices in each cycle reaches a constant value (video 2 in Supplementary Materials shows the typical equilibrium vortex lattice observed [22]). This means that as the nullclines begin to entangle, they create new vortices, which in turn have their own nullclines that also begin to entangle. This, as a kind of nullcline weaving process (see video 1 in Supplementary Materials shows the vortex lattice emergence [22]), forms the vortex lattice, as illustrated in Figs. 1, 3, and 4. Note that ω_{TT} is of the order of hundredths of Hertz. The number of vortices of the lattice $\langle N_v \rangle$ was measured stroboscopically and remains constant as a given frequency ω . Fig. 4 illustrates how a snapshot is taken at each maximum (minimum) of the driven voltage and, with a suitable programme, the number of vortices N_v is determined—*stroboscopic measurement* (see video 2 in Supplementary Materials shows the stroboscopic measurement considering the maximum or minimum of the driven voltage [22]). Fig. 5a summarises how the average number of vortices $\langle N_v \rangle$ changes as a function of frequency ω . This chart suggests that the number of vortices increases

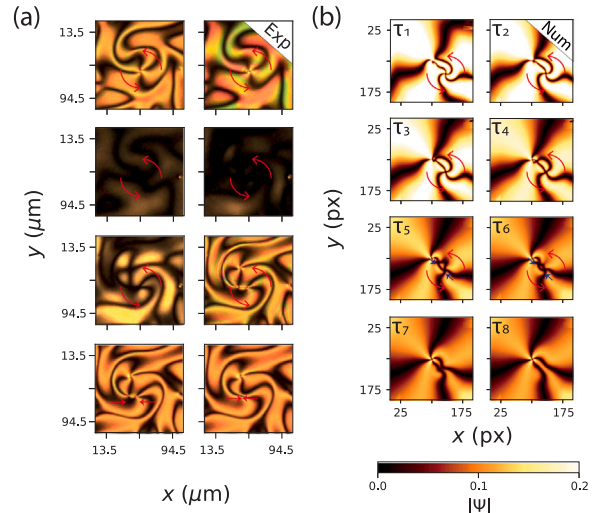


Fig. 3. Dynamics of experimental and theoretical nullcline curves entanglement. (a) Experimental time series of snapshots showing a positive topological defect generating a pair of vortices by nullcline entanglement ($t_1 < t_2 < t_3 < t_4 < t_5 < t_6 < t_7 < t_8$). Due to the crossed polarisers configuration of the microscope, the nullcline entanglement is difficult to observe experimentally when the molecular average is on the vertical configuration (homeotropic state). Namely, at this point in time, the liquid crystal molecules are oriented almost perpendicular to the plates. Figure (b) depicts the results of a numerical simulation, the colour scale of which can be modified to facilitate the visualisation of this particular feature. ($\tau_1 < \tau_2 < \tau_3 < \tau_4 < \tau_5 < \tau_6 < \tau_7 < \tau_8$). Since the topological charge must be conserved, the two new vortices always have a charge of opposite sign, and in some cases, the negative vortex annihilates with the initial positive vortex. In the numerical simulation, the colourmap accounts for the polarisation field $\psi = Re(A)Im(A)$ obtained from Eq. (7) with $\tilde{I} = 1.0$, $\gamma = 2.0$, $\mu = 1.2$, $K_3 = 6.0$, $\delta = 1.5$, $\sigma = 2.3$, $m = 1.5$, and $b_0 = 2.0$.

continuously as the nullclines begin to touch. Therefore, the system undergoes a topological transition out of equilibrium at the frequency $\omega = \omega_{TT}$. In fact, for $\omega < \omega_{TT}$, the system permanently shows vortices. For even more minor frequencies, electroconvection (emergence of roll-type patterns) begins to dominate, disturbing or stopping the vortex lattice's growth. Electroconvection is a phenomenon that allows the generation of domains whose boundary vortices are generated. The characteristic width of these domains varies in a relatively proportional manner with frequency, which causes the number of vortices to change.

To clarify the nature of the topological transition type, we have performed several cycles of decreasing and increasing the frequency near the critical frequency ω_{TT} ; we have not observed any hysteresis phenomenon (see Fig. 5). Hence, this analysis suggests that the transition is supercritical in nature. As a result of the interaction among the dancing vortices, the system exhibits a square vortex lattice surrounding the central vortex (see Fig. 1). Similar patterns have been observed when a similar system is subjected to thermal gradients [17]. Additional vortices are assimilated into this square vortex lattice when the frequency is decreased. Experimentally, we have characterised the phase space diagram in which the topological transition and emergence of a topological vortex lattice are observed by varying the frequency and voltage (cf. Fig. 2). Note that the critical frequency $\omega_{TT}(V_0)$ decreases as a function of the applied voltage V_0 .

4. Theoretical description close to reorientation instability

The director vector field $\vec{n}(\vec{r}, t)$ can describe the molecular orientation at a fixed temperature [5,9]. The dynamic evolution of the director is characterised by minimising the Frank–Oseen free energy

$$F = \frac{1}{2} \int \left\{ K_1 (\nabla \cdot \vec{n})^2 + K_2 (\vec{n} \cdot (\nabla \times \vec{n}))^2 - \epsilon_a (\vec{n} \cdot \vec{E})^2 + K_3 (\vec{n} \times (\nabla \times \vec{n}))^2 - \chi_a (\vec{n} \cdot \vec{B})^2 \right\} dV, \quad (1)$$

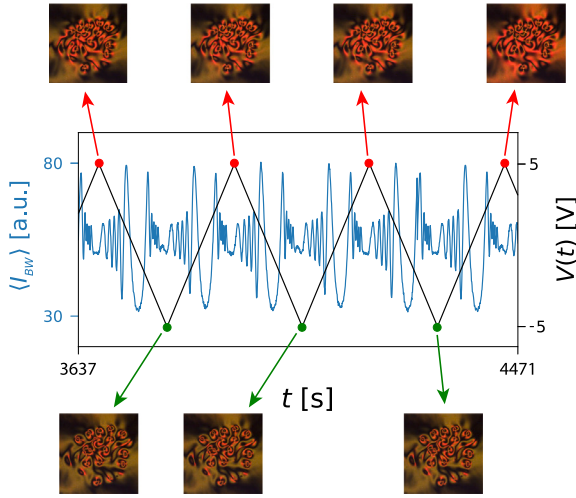


Fig. 4. Stroboscopic measurement of the number of vortices N_v in a liquid crystal cell with a magnetic ring and an oscillating electric field. Temporal evolution of the transmitted light intensity $I_{BW}(t)$ (blue curve) and voltage applied $V(t)$ (black curve) to the liquid crystal sample. The number of vortices N_v is counted when the driven voltage $V(t)$ reaches maximum (minimum) values. The red and green dots represent the maximum and minimum of the driven voltage, respectively. The insets show the snapshots acquired at the respective driven voltage extremes. (For interpretation of the references to colour in this figure legend, the reader is referred to the web version of this article.)

where K_1 , K_2 , and K_3 are the elastic constants related to the distortions of splay, twist, and bend, respectively, ϵ_a and χ_a are the dielectric and magnetic anisotropy constants, $\vec{E} = E_z(t)\hat{z} = -V_\omega(t)/d\hat{z}$ is the oscillatory vertical electric field, and $\vec{B} = B_r\hat{r} + B_z\hat{z}$ is the magnetic field generated by the magnet ring [19], which has the explicit form

$$\vec{B}(r, z) = m_0 \left[\frac{3zr\hat{r} + (3z^2 + \sigma)\hat{z}}{(r^2 + z^2)^{5/2}} - \frac{\ell_0\hat{z}}{(r^2 + z^2)^{3/2}} \right], \quad (2)$$

where $\sigma > 0$ and ℓ_0 are phenomenological parameters (m^2 and dimensionless, respectively) that account for the geometric features of the magnet ring, m_0 is a constant that has a dimension of permeability per magnetic moment, $\{z, r, \theta\}$ are the cylindrical coordinates, and z accounts for the vertical coordinate of the NLCC. The origin of the coordinate is fixed at the centre of the magnet ring. Note that due to the azimuthal symmetry of the ring, the magnetic field does not depend on the θ coordinate.

The director dynamics is characterised by the minimisation of the free energy \mathcal{F} with the constraint that the conservation norm of the director ($\|\vec{n}\|^2 = 1$), then the director satisfies [9]

$$I \frac{d^2 \vec{n}}{dt^2} + \gamma \frac{d\vec{n}}{dt} = -\frac{\delta \mathcal{F}}{\delta \vec{n}} + \vec{n} \left(\vec{n} \cdot \frac{\delta \mathcal{F}}{\delta \vec{n}} \right) - 2\vec{n} \left(\frac{d\vec{n}}{dt} \right)^2, \quad (3)$$

where γ and I are the director's rotational viscosity and inertia moment. Meanwhile, the first and second terms of the left-hand side account for the inertial and viscous torque on the director. The last terms on the right-hand side guarantee the preservation of the director norm [23]. Note that the inertial term is usually neglected because the liquid crystal is a viscous medium. Hence, the dynamics of the directors can be approximated by (viscous torque dynamics)

$$\gamma \frac{d\vec{n}}{dt} = -\frac{\delta \mathcal{F}}{\delta \vec{n}} + \vec{n} \left(\vec{n} \cdot \frac{\delta \mathcal{F}}{\delta \vec{n}} \right). \quad (4)$$

Due to the complexity of Eq. (4), analytical studies are of greater complexity, to provide greater analytical and intuitive insights, we use the strategy of considering the dynamics of the director around the

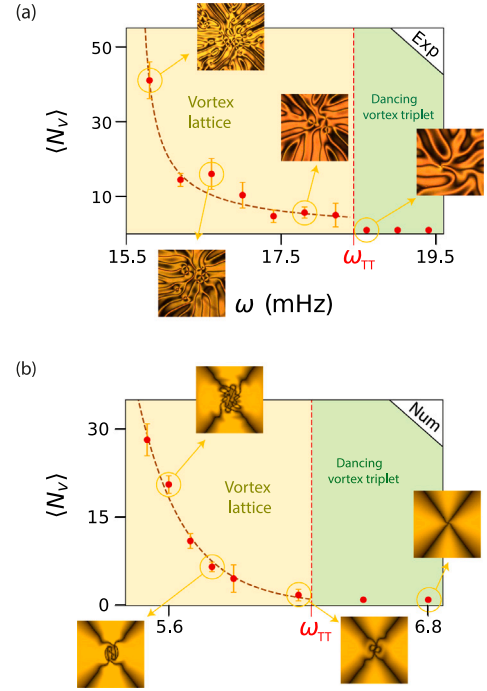


Fig. 5. Bifurcation diagram of the number of vortices $\langle N_v \rangle$ as a function of the frequency ω of the driven voltage for (a) experimental and (b) numerical data. ω_{TT} is the critical frequency at which the topological transition is observed. The coloured regions, yellow and green, represent the region of vortex lattices and triplets. The insets show the typical images of the central region fixed by the magnet (a) and the numerical simulation (b). A topological transition can be observed at $\omega_{TT} = 18$ mHz for $V_0 = 15$ V_{pp}, which is numerically reproduced using Eq. (7) with $\bar{I} = 1.0$, $\gamma = 2.0$, $\mu = 1.2$, $K_3 = 6.0$, $\delta = 1.5$, $\sigma = 2.3$, $m = 1.5$, and $b_0 = 2.0$. (For interpretation of the references to colour in this figure legend, the reader is referred to the web version of this article.)

reorientation instability [24], then considering the ansatz

$$\vec{n}(r, \theta, z) \approx \begin{pmatrix} \text{Re}(A) \sin\left(\frac{\pi z}{d}\right) \\ \text{Im}(A) \sin\left(\frac{\pi z}{d}\right) \\ 1 - \frac{|A|^2}{2} \sin^2\left(\frac{\pi z}{d}\right) \end{pmatrix} + h.o.t., \quad (5)$$

where $A(r, \theta)$ is the complex amplitude of the critical spatial mode describing the projection of the director field onto the horizontal plane, d is the thickness of the cell, and *h.o.t.* accounts for the higher-order terms in A .

Using the ansatz (5) on the equation for the molecular director evolution (4) and after straightforward calculations, one gets the amplitude equation (see the details in the Methods Section)

$$\gamma \partial_t A = \mu(t)A - aA|A|^2 + \nabla_\perp^2 A + \delta \partial_{\eta\eta} \bar{A} + f(r)e^{i\theta}, \quad (6)$$

where $\mu(t) = -K_3(\pi/d)^2 - \epsilon_a E_z^2(t) - \chi_a B_z^2(r)$ is the bifurcation parameter, for the sake of simplicity, we consider a harmonic electric field $E_z(t) = -E_0 \cos(\omega t)$, $\delta = (K_1 - K_2)/(K_1 + K_2)$ is the constant that accounts for the anisotropic coupling of the liquid crystal, the cubic coefficient a is defined by $a = (2K_1 - 3K_3)\pi^2/2d^2 - 3\epsilon_a E^2/4 - 3\chi_a B_z^2/4$, $\partial_\eta \equiv \partial_{x'} + i\partial_{y'}$ is the Wirtinger derivative where the spatial coordinates have been rescaled $r' \rightarrow \bar{r}\sqrt{2/(K_1 + K_2)}$ (see Appendix), which is a differential operator in the complex plane, $\nabla_\perp^2 = \partial_{\eta\eta}$ is the Laplacian operator, and $f(r) = -4\chi_a a^{1/2} B_r(r, z = d/2)B_z(r, z = d/2)/\pi$ stands for the topological forcing induced by the magnetic ring. The model Eq. (6) is valid in the limit $\mu \ll 1$, $A \sim \mu^{1/2}$, $\partial_\eta \sim \mu^{1/2}$, $f(r) \sim \mu^{3/2}$, and $\partial_t \sim \mu/\gamma$. All the terms of Eq. (6) are considered of the same order for this multi-scale.

Numerical simulations of the amplitude Eq. (6), with an oscillating electric field at frequencies of order 1, show the emergency and annihilation of vortices, giving rise to a vortex triplet. At low frequencies, numerical simulations only show a dancing vortex triplet [20]; the

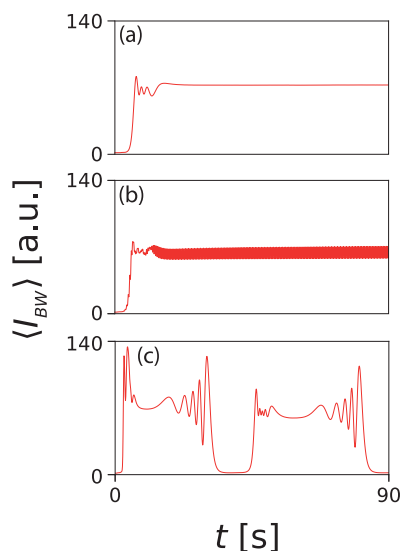


Fig. 6. Overdamped and damped oscillation dynamics of the light intensity transmitted by the liquid crystal cell with a magnetic ring and oscillating electric field for different frequencies. The CMOS camera measures the average intensity of light transmitted by the liquid crystal cell with crossed polarisers I_{BW} in grayscale as a function of time for (a) 100 Hz, (b) 1 Hz, and (c) 0.01 Hz.

nullclines around the vortex rotate and follow the core dynamics of the vortex but never entangle. This phenomenon is observed experimentally at larger frequencies on the order of Hertz. Thus, the amplitude Eq. (6) does not account for the entanglement of the nullclines and the emergence of the vortex lattice as observed experimentally. The nullclines can be entangled if the director $\bar{n}(\vec{r}, t)$ presents a dynamic with greater freedom than that imposed by the overdamped system. Furthermore, the vortex annihilation interaction that governs the model Eq. (6) must be changed to emerge a stable vortex lattice. Therefore, phenomenologically, we will include inertial effects in the dynamics of the amplitude equation to modify the dynamics of nullclines and the vortex interactions.

5. Phenomenological model for nullclines entanglement and topological transitions

Let us consider the model

$$\bar{I} \partial_{tt} A + \gamma \partial_t A = \mu A - aA|A|^2 + \nabla_{\perp}^2 A + \delta \partial_{\eta\eta} \bar{A} + f(r)e^{i\theta}, \quad (7)$$

where \bar{I} accounts for the inertia in the amplitude equation. This inertia term may be originated by several phenomena associated with the low-frequency regime, such as rotational inertia of the material [9], electroconvection [5], charge accumulation, and liquid crystal motion [25–27]. However, the origin of this term in our experiment is not established. Despite this, there is evidence that the system does not behave fully dissipative (overdamping) in the frequency range of this experiment, as illustrated in Fig. 6. Note that the intensity is a function of the orientation of the director $\bar{n}(\vec{r}, t)$. From these charts, one can infer that for frequencies of the order of 1 Hz and higher, the system reaches a stable state in which the molecular average orientation \bar{n} relaxes in an overdamped manner to equilibrium. However, the average molecular reorientation for lower frequencies presents damped oscillations forward to equilibrium. For frequencies on the order of 10 mHz or smaller, the relaxation time is of the same order as the period of the driven voltage, which is associated with inertial effects that are not present in the high-frequency regime (cf. Fig. 6c).

Numerical simulations of Eq. (7) for high frequencies show as an equilibrium, a triplet of vortices [19]. When a noisy initial condition is considered, which accounts for inherent thermal fluctuations of the

physical system, a large nucleation of vortices is observed, which subsequently begin to annihilate by pairs with opposite topological charges. Finally, the system reaches the triplet as equilibrium. This dynamic is similar to that observed experimentally [19]. As the voltage frequency decreases, the vortices dance; the nullcline curves begin to unfold oscillatory [20]. As the frequency is further reduced, the associated nullclines begin to entangle and generate new vortices. Fig. 3b illustrates the typical dynamics observed numerically (see video 1 on the Supplementary Materials [22]). Note that the observed dynamics are similar to the experimental ones. Likewise, the number of vortices (N_v) measured stroboscopically remains constant as a given frequency ω , similar to what was observed experimentally. Fig. 5b shows the bifurcation diagram obtained using Eq. (7). Hence, the amplitude Eq. (7) with inertia and time- and space-dependent parameters shows a topological transition out of equilibrium as the frequency decreases. The numerical observations show a qualitative agreement with the experimental ones.

6. Conclusions

Non-equilibrium systems present topological transitions sustained by the injection and dissipation of energy. Based on the complex dynamics of nullcline curves associated with vortices, we have established, experimentally and theoretically, the emergence of dissipative vortex lattices. Combining a magnetic ring and an oscillating electric field allowed us to observe a vortex lattice. We note that the vortex lattice persists when removing the magnet below the topological transition point ω_{TT} , a phenomenon similar to that already observed experimentally [18]. The observed vortex lattices have a square structure. These structures are a consequence of the interaction of vortices. However, the interaction of dancing vortices is an open problem that needs to be solved to figure out dissipative vortex lattices. The mechanism found is generic and can be observed in other oscillatory-driven physical systems, such as magnetic systems, Bose–Einstein condensates, superconductors, and fluids, to name a few.

The inertia in the amplitude equation (7) is a fundamental phenomenological ingredient for the observed dynamics. Other approaches that generate nullcline rotation and oscillation include the use of imaginary [28] or time-dependent [20] coefficients in the Ginzburg–Landau equation. However, nullcline entanglement on these models is not shown, and therefore, they are not consistent with the observations made in our system.

Unfortunately, there are no experimental studies on the director inertia in liquid crystals as a function of frequency (fractions of hertz) and temperature, which would allow us to be certain of the origin of this term in the phenomenological model. If one does not neglect the inertial torque of the director Eq. (3), one can derive the amplitude Eq. (7) directly from Eq. (3), where $I = \bar{I}$ (see Methods Section). However, this kind of term is expected to be important for significant frequencies (of the order of THz) and not for small ones. For inertia to be considered in the multi-scaling of the amplitude Eq. (7), $\bar{I} \sim \gamma^2/\mu$ must be satisfied. Theoretically, taking into account the friction between the molecules and not considering the frequency of the electric field, the estimation of $\gamma \approx 3 \times 10^{-3}$ erg s/cm³ = 0.3 mPa s [29]. However, the liquid crystal under study has a viscosity of 4 orders of magnitude greater, $\gamma = 204$ mPa s, which is consistent with the experimentally reported viscosity of nematic liquid crystals [30]. Due to $\gamma \ll 1$ (in Pa s unit), the inertia of the director must be smaller or of the order of γ ; however, in simple estimates, ignoring the collective effect of the molecules and the presence of an oscillating field at slow frequency, it is found to be several orders of magnitude smaller [29]. On the other hand, the appearance of inertia may result from charge motion and backflow. Note that at low frequencies, charge motion can be generated due to the weak anisotropic conductivity of the liquid crystal [5], which can play an important role in the behaviour of inertia $\bar{I}(\omega)$ and viscosity $\gamma(\omega)$. Likewise, low frequencies can generate backflow, in which director evolution is coupled with fluid dynamics, where

inertia must also be included (see Ericksen–Leslie theory [9]). Standing waves with self-adaptation to driving frequencies have recently been discovered in homeotropic sandwich cells filled with chiral nematics with negative dielectric anisotropy [31]. Likewise, travelling waves resulting from the reorientation of the director have been observed in liquid crystal samples induced by the wave of the pulse train [32]. Inertial torque is fundamental in understanding waves in liquid crystals and nullclines dynamics.

CRedit authorship contribution statement

Marcel G. Clerc: Formal analysis, Investigation, Project administration, Supervision, Writing – original draft. **R. Gajardo-Pizarro:** Data curation, Formal analysis, Investigation, Methodology, Writing – review & editing.

Declaration of competing interest

The authors declare that they have no known competing financial interests or personal relationships that could have appeared to influence the work reported in this paper.

Data availability

Data will be made available on request.

Acknowledgements

M.G.C. and R.G-P. are thankful for the financial support of ANID-Millennium Science Initiative Program-ICN17_012 (MIRO) and FONDECYT 1210353 project. R.G-P. thanks the financial support of ANID by Beca Doctorado Nacional 2022-21221819.

Appendix. Derivation of amplitude equation with inertia

Using the Frank–Oseen free energy (1) in the director Eq. (3), one gets

$$I \frac{d^2 \bar{n}}{dt^2} + \gamma \frac{d \bar{n}}{dt} = K_3 [\nabla^2 \bar{n} - \bar{n}(\bar{n} \cdot (\nabla^2 \bar{n})) + (K_3 - K_1) [\bar{n}(\bar{n} \cdot \nabla)(\nabla \cdot \bar{n}) - \nabla(\nabla \cdot \bar{n}) + (K_2 - K_3) [2(\bar{n} \cdot (\nabla \times \bar{n}))(\bar{n}(\bar{n} \cdot (\nabla \times \bar{n})) - (\nabla \times \bar{n})) + (\bar{n} \times (\nabla(\bar{n} \cdot (\nabla \times \bar{n}))))] - \epsilon_a (\bar{E} \cdot \bar{n})(\bar{n}(\bar{E} \cdot \bar{n}) - \bar{E}) - \chi_a (\bar{B} \cdot \bar{n})(\bar{n}(\bar{B} \cdot \bar{n}) - \bar{B})].$$

Close to the transition point, it is possible to suppose that $\bar{n} \approx (n_1, n_2, 1 - \frac{n_1^2 + n_2^2}{2})$. With this approximation, the above equation reads

$$I \ddot{n}_1 + \gamma \dot{n}_1 = K_3 \left[\nabla^2 n_1 + n_1 \left((\partial_z n_1)^2 + (\partial_z n_2)^2 \right) - (K_3 - K_1) \left[\frac{1}{2} n_1 \partial_{zz} (n_1^2 + n_2^2) + \partial_{xx} n_1 + \partial_{xy} n_2 \right] + (K_2 - K_3) [\partial_{yy} n_1 - \partial_{xy} n_2] - \epsilon_a n_1 E_z^2 (1 - n_1^2 - n_2^2) - \epsilon_a (2n_1^2 E_x E_x + 2n_1 n_2 E_x E_y - E_x E_z (1 - \frac{1}{2} (n_1^2 + n_2^2))) - \chi_a n_1 B_z^2 (1 - n_1^2 - n_2^2) - \chi_a (2n_1^2 B_x B_x + 2n_1 n_2 B_x B_y - B_x B_z (1 - \frac{1}{2} (n_1^2 + n_2^2))), \right. \quad (8)$$

$$I \ddot{n}_2 + \gamma \dot{n}_2 = K_3 \left[\nabla^2 n_2 + n_2 \left((\partial_z n_1)^2 + (\partial_z n_2)^2 \right) - (K_3 - K_1) \left[\frac{1}{2} n_2 \partial_{zz} (n_1^2 + n_2^2) + \partial_{xy} n_1 + \partial_{yy} n_2 \right] + (K_2 - K_3) [-\partial_{xy} n_1 + \partial_{xx} n_2] - \epsilon_a n_2 E_z^2 (1 - n_1^2 - n_2^2) - \epsilon_a (2n_2^2 E_x E_x + 2n_1 n_2 E_x E_y - E_y E_z (1 - \frac{1}{2} (n_1^2 + n_2^2))) - \chi_a n_2 B_z^2 (1 - n_1^2 - n_2^2) - \chi_a (2n_2^2 B_x B_x + 2n_1 n_2 B_x B_y - B_y B_z (1 - \frac{1}{2} (n_1^2 + n_2^2))), \right. \quad (9)$$

$$+ n_2^2)) - \chi_a n_2 B_z^2 (1 - n_1^2 - n_2^2) - \chi_a (2n_2^2 B_x B_x + 2n_1 n_2 B_x B_y - B_y B_z (1 - \frac{1}{2} (n_1^2 + n_2^2))), \quad (9)$$

First, we consider the linear terms in n_1 and n_2 to analyse the linear instability and using $\bar{E} = E \hat{z} = \frac{V}{d} \hat{z}$ and $\bar{B} = B_x \hat{x} + B_y \hat{y} + B_z \hat{z}$, we obtain

$$I \ddot{n}_1 + \gamma \dot{n}_1 = K_3 \partial_{zz} n_1 - \epsilon_a n_1 E^2 - \chi_a n_1 B_z^2, \quad (10)$$

$$I \ddot{n}_2 + \gamma \dot{n}_2 = K_3 \partial_{zz} n_2 - \epsilon_a n_2 E^2 - \chi_a n_2 B_z^2. \quad (10)$$

Considering the homeotropic boundary conditions, $n_1(z=0) = n_1(z=d) = n_2(z=0) = n_2(z=d) = 0$, and the ansatz

$$\begin{pmatrix} n_1(x, t) \\ n_2(x, t) \end{pmatrix} = e^{\sigma t} \begin{pmatrix} n_1^0 \\ n_2^0 \end{pmatrix} \sin\left(\frac{\pi l}{d} z\right),$$

l is an integer number. Using the previous ansatz in the linear Eq. (10), one gets the linear growth rate

$$\sigma_\ell = -\frac{\gamma}{2I} \pm \sqrt{\left(\frac{\gamma}{2I}\right)^2 - \frac{\alpha_\ell}{I}}, \quad (11)$$

where $\alpha_\ell = K_3 \frac{\pi^2 l^2}{d^2} + \epsilon_a E^2 + \chi_a B_z^2$. The destabilisation condition is $\sigma_\ell = 0$ which corresponds to the reorientation instability; then, we obtain the critical voltage

$$V_c = -E_c d = \sqrt{-\frac{K_3 \pi^2}{\epsilon_a} - \frac{\chi_a B_z^2 d^2}{\epsilon_a}}, \quad (12)$$

for the unstable mode $l = 1$.

To understand the evolution around orientational instability, let us consider the following weakly nonlinear analysis based on the ansatz

$$\bar{n} = \begin{pmatrix} X(x, y, t) \sin\left(\frac{\pi z}{d}\right) \\ Y(x, y, t) \sin\left(\frac{\pi z}{d}\right) \end{pmatrix} + \begin{pmatrix} W_1 \\ W_2 \end{pmatrix},$$

where $X(x, y, t)$ and $Y(x, y, t)$ account for the amplitude of the critical mode, W_1 and W_2 stands for higher order corrections of the linear mode. Introducing the notation $\bar{E} = E \hat{z}$ and $\bar{B} = B_x \hat{x} + B_y \hat{y} + B_z \hat{z}$, and employing the previous ansatz in Eqs. (8) and (9), we get

$$I \dot{X} \sin\left(\frac{\pi z}{d}\right) + \gamma \dot{X} \sin\left(\frac{\pi z}{d}\right) = (K_3 \partial_{zz} - \epsilon_a E^2 - \chi_a B_z^2) W_1 + K_3 \left[\left(\nabla_\perp^2 X - \frac{\pi^2}{d^2} X \right) \sin\left(\frac{\pi z}{d}\right) + \frac{\pi^2}{d^2} X (X^2 + Y^2) \sin\left(\frac{\pi z}{d}\right) \cos^2\left(\frac{\pi z}{d}\right) \right] - (K_3 - K_1) \left[\partial_{xx} X \sin\left(\frac{\pi z}{d}\right) + \partial_{xy} Y \sin\left(\frac{\pi z}{d}\right) \right] + \frac{\pi^2}{d^2} X (X^2 + Y^2) \sin\left(\frac{\pi z}{d}\right) \left(\cos^2\left(\frac{\pi z}{d}\right) - \sin^2\left(\frac{\pi z}{d}\right) \right) + (K_2 - K_3) \left[\partial_{yy} X \sin\left(\frac{\pi z}{d}\right) - \partial_{xy} Y \sin\left(\frac{\pi z}{d}\right) \right] - \epsilon_a E^2 X \sin\left(\frac{\pi z}{d}\right) \left[1 - (X^2 + Y^2) \sin^2\left(\frac{\pi z}{d}\right) \right] - \chi_a B_z^2 X \sin\left(\frac{\pi z}{d}\right) \left[1 - (X^2 + Y^2) \sin^2\left(\frac{\pi z}{d}\right) \right] - \chi_a \left[2B_x B_z X^2 \sin^2\left(\frac{\pi z}{d}\right) + 2B_y B_z XY \sin^2\left(\frac{\pi z}{d}\right) - B_x B_z \left(1 - \frac{X^2 + Y^2}{2} \sin^2\left(\frac{\pi z}{d}\right) \right) \right], \quad (13)$$

$$I \dot{Y} \sin\left(\frac{\pi z}{d}\right) + \gamma \dot{Y} \sin\left(\frac{\pi z}{d}\right) = (K_3 \partial_{zz} - \epsilon_a E^2 - \chi_a B_z^2) W_2 + K_3 \left[\left(\nabla_\perp^2 Y - \frac{\pi^2}{d^2} Y \right) \sin\left(\frac{\pi z}{d}\right) + \frac{\pi^2}{d^2} Y (X^2 + Y^2) \sin\left(\frac{\pi z}{d}\right) \cos^2\left(\frac{\pi z}{d}\right) \right] - (K_3 - K_1) \left[\partial_{xy} X \sin\left(\frac{\pi z}{d}\right) + \partial_{yy} Y \sin\left(\frac{\pi z}{d}\right) \right] + \frac{\pi^2}{d^2} Y (X^2 + Y^2) \sin\left(\frac{\pi z}{d}\right) \left(\cos^2\left(\frac{\pi z}{d}\right) - \sin^2\left(\frac{\pi z}{d}\right) \right) + \frac{\pi^2}{d^2} Y (X^2 + Y^2) \sin\left(\frac{\pi z}{d}\right) \left(\cos^2\left(\frac{\pi z}{d}\right) - \sin^2\left(\frac{\pi z}{d}\right) \right) \right]$$

$$\begin{aligned}
&+(K_2 - K_3) \left[\partial_{xx} Y \sin\left(\frac{\pi z}{d}\right) - \partial_{xy} X \sin\left(\frac{\pi z}{d}\right) \right] \\
&-\varepsilon_a E^2 Y \sin\left(\frac{\pi z}{d}\right) \left[1 - (X^2 + Y^2) \sin^2\left(\frac{\pi z}{d}\right) \right] \\
&-\chi_a B_z^2 Y \sin\left(\frac{\pi z}{d}\right) \left[1 - (X^2 + Y^2) \sin^2\left(\frac{\pi z}{d}\right) \right] \\
&-\chi_a \left[2B_y B_z Y^2 \sin^2\left(\frac{\pi z}{d}\right) + 2B_x B_z X Y \sin^2\left(\frac{\pi z}{d}\right) \right. \\
&\left. - B_y B_z \left(1 - \frac{X^2 + Y^2}{2} \sin^2\left(\frac{\pi z}{d}\right) \right) \right]. \tag{14}
\end{aligned}$$

This equation can be rewritten in the form

$$\mathcal{L}\vec{W} = \begin{pmatrix} I\ddot{X} \sin\left(\frac{\pi z}{d}\right) + \gamma\dot{X} \sin\left(\frac{\pi z}{d}\right) - \Phi_1 \\ I\ddot{Y} \sin\left(\frac{\pi z}{d}\right) + \gamma\dot{Y} \sin\left(\frac{\pi z}{d}\right) - \Phi_2 \end{pmatrix},$$

Where the linear operator acting on \vec{W} is

$$\mathcal{L} = \begin{pmatrix} K_3 \partial_{zz} - \varepsilon_a E^2 - \chi_a B_z^2 & 0 \\ 0 & K_3 \partial_{zz} - \varepsilon_a E^2 - \chi_a B_z^2 \end{pmatrix}. \tag{15}$$

Introducing the inner product $\langle f|g \rangle = \int_0^d f(z)g(z)dz$, the operator \mathcal{L} is self-adjoint ($\mathcal{L} = \mathcal{L}^\dagger$). The kernel of this operator is of dimension two, characterised by the vectorial functions $\text{Ker}(\mathcal{L}^\dagger) = \{\vec{v}_1 = (\sin(\pi z/d), 0); \vec{v}_2 = (0, \sin(\pi z/d))\}$. To solve the linear equation (15), we apply the Fredholm alternative for each element of the kernel of \mathcal{L}^\dagger , we obtain the two following equations

$$\begin{aligned}
\left\langle I\dot{X} \sin\left(\frac{\pi z}{d}\right) + \gamma\dot{X} \sin\left(\frac{\pi z}{d}\right) - \Phi_1 \middle| \sin\left(\frac{\pi z}{d}\right) \right\rangle &= 0, \\
\left\langle I\dot{Y} \sin\left(\frac{\pi z}{d}\right) + \gamma\dot{Y} \sin\left(\frac{\pi z}{d}\right) - \Phi_2 \middle| \sin\left(\frac{\pi z}{d}\right) \right\rangle &= 0
\end{aligned}$$

Making explicit the coefficients Φ_1 and Φ_2 , these equations read

$$\begin{aligned}
(I\ddot{X} + \gamma\dot{X}) \frac{d}{2} &= K_3 \left[\left(\nabla_\perp^2 X - \frac{\pi^2}{d^2} X \right) \int_0^d \sin^2\left(\frac{\pi z}{d}\right) dz \right. \\
&+ \left. \frac{\pi^2}{d^2} X (X^2 + Y^2) \int_0^d \sin^2\left(\frac{\pi z}{d}\right) \cos^2\left(\frac{\pi z}{d}\right) dz \right] \\
&-(K_3 - K_1) \left[(\partial_{xx} X + \partial_{xy} Y) \int_0^d \sin^2\left(\frac{\pi z}{d}\right) dz \right. \\
&+ \left. \frac{\pi^2}{d^2} X (X^2 + Y^2) \int_0^d \sin^2\left(\frac{\pi z}{d}\right) \left(\cos^2\left(\frac{\pi z}{d}\right) - \sin^2\left(\frac{\pi z}{d}\right) \right) dz \right] \\
&+(K_2 - K_3) (\partial_{yy} X - \partial_{xy} Y) \int_0^d \sin^2\left(\frac{\pi z}{d}\right) dz \\
&-\varepsilon_a E^2 X \left[\int_0^d \sin^2\left(\frac{\pi z}{d}\right) dz - (X^2 + Y^2) \int_0^d \sin^4\left(\frac{\pi z}{d}\right) dz \right] \\
&-\chi_a X \left[\int_0^d B_z^2(z) \sin^2\left(\frac{\pi z}{d}\right) dz - (X^2 + Y^2) \int_0^d B_z^2(z) \sin^4\left(\frac{\pi z}{d}\right) dz \right] \\
&-\chi_a \left[2X^2 \int_0^d B_x(z) B_z(z) \sin^3\left(\frac{\pi z}{d}\right) dz \right. \\
&+ 2XY \int_0^d B_y(z) B_z(z) \sin^3\left(\frac{\pi z}{d}\right) dz \\
&- \int_0^d B_x(z) B_z(z) \sin\left(\frac{\pi z}{d}\right) dz \\
&+ \left. \frac{X^2 + Y^2}{2} \int_0^d B_x(z) B_z(z) \sin^3\left(\frac{\pi z}{d}\right) dz \right], \tag{16}
\end{aligned}$$

$$\begin{aligned}
(I\ddot{Y} + \gamma\dot{Y}) \frac{d}{2} &= K_3 \left[\left(\nabla_\perp^2 Y - \frac{\pi^2}{d^2} Y \right) \int_0^d \sin^2\left(\frac{\pi z}{d}\right) dz \right. \\
&+ \left. \frac{\pi^2}{d^2} Y (X^2 + Y^2) \int_0^d \sin^2\left(\frac{\pi z}{d}\right) \cos^2\left(\frac{\pi z}{d}\right) dz \right] \\
&-(K_3 - K_1) \left[(\partial_{xy} X + \partial_{yy} Y) \int_0^d \sin^2\left(\frac{\pi z}{d}\right) dz \right. \\
&+ \left. \frac{\pi^2}{d^2} Y (X^2 + Y^2) \int_0^d \sin^2\left(\frac{\pi z}{d}\right) \left(\cos^2\left(\frac{\pi z}{d}\right) - \sin^2\left(\frac{\pi z}{d}\right) \right) dz \right]
\end{aligned}$$

$$\begin{aligned}
&+(K_2 - K_3) (\partial_{xx} Y - \partial_{xy} X) \int_0^d \sin^2\left(\frac{\pi z}{d}\right) dz \\
&-\varepsilon_a E^2 Y \left[\int_0^d \sin^2\left(\frac{\pi z}{d}\right) dz - (X^2 + Y^2) \int_0^d \sin^4\left(\frac{\pi z}{d}\right) dz \right] \\
&-\chi_a Y \left[\int_0^d B_z^2(z) \sin^2\left(\frac{\pi z}{d}\right) dz - (X^2 + Y^2) \int_0^d B_z^2(z) \sin^4\left(\frac{\pi z}{d}\right) dz \right] \\
&-\chi_a \left[2Y^2 \int_0^d B_y(z) B_z(z) \sin^3\left(\frac{\pi z}{d}\right) dz \right. \\
&+ 2XY \int_0^d B_x(z) B_z(z) \sin^3\left(\frac{\pi z}{d}\right) dz \\
&- \int_0^d B_y(z) B_z(z) \sin\left(\frac{\pi z}{d}\right) dz \\
&+ \left. \frac{X^2 + Y^2}{2} \int_0^d B_y(z) B_z(z) \sin^3\left(\frac{\pi z}{d}\right) dz \right]. \tag{17}
\end{aligned}$$

Considering that B_x , B_y , and B_z are slowly varying functions of z , integrating the previous expressions after straightforward calculations, we obtain

$$\begin{aligned}
I\ddot{X} + \gamma\dot{X} &= \left(-\frac{K_3 \pi^2}{d^2} - \varepsilon_a E^2 - \chi_a B_z^2 \right) X \\
&- \left(\frac{(2K_1 - 3K_3)\pi^2}{2d^2} - \frac{3\varepsilon_a E^2}{4} - \frac{3\chi_a B_z^2}{4} \right) X (X^2 + Y^2) \\
&+ K_1 (\nabla_\perp^2 X - \partial_{yy} X + \partial_{xy} Y) \\
&+ K_2 (\nabla_\perp^2 X - \partial_{xx} X - \partial_{xy} Y) - \frac{4\chi_a}{\pi} B_x B_z, \\
I\ddot{Y} + \gamma\dot{Y} &= \left(-\frac{K_3 \pi^2}{d^2} - \varepsilon_a E^2 - \chi_a B_z^2 \right) Y \\
&- \left(\frac{(2K_1 - 3K_3)\pi^2}{2d^2} - \frac{3\varepsilon_a E^2}{4} - \frac{3\chi_a B_z^2}{4} \right) Y (X^2 + Y^2) \\
&+ K_1 (\nabla_\perp^2 Y - \partial_{xx} Y + \partial_{xy} X) \\
&+ K_2 (\nabla_\perp^2 Y - \partial_{yy} Y - \partial_{xy} X) - \frac{4\chi_a}{\pi} B_y B_z. \tag{18}
\end{aligned}$$

Introducing the variable $A = X + iY$, the definitions $B_x + iB_y = B_\rho e^{i\theta}$, $\partial_\eta = \partial_x + i\partial_y$, $\mu = -K_3 \pi^2/d^2 - \varepsilon_a E^2 - \chi_a B_z^2$, $a = (2K_1 - 3K_3)\pi^2/2d^2 - 3\varepsilon_a E^2/4 - 3\chi_a B_z^2/4$, $\delta = (K_1 - K_2)/(K_1 + K_2)$ and $f(r) = -\frac{4\chi_a}{\pi} B_\rho(r) B_z$, and rescaling the space $\vec{r}' = \sqrt{2/(K_1 + K_2)} \vec{r}$, in the previous equation, we get [the phenomenological amplitude Eq. (7)]

$$I\partial_{tt} A + \gamma\partial_t A = \mu A - aA|A|^2 + \nabla_\perp^2 A + \delta\partial_{\eta\eta} \bar{A} + f(r)e^{i\theta}. \tag{19}$$

Considering the overdamped limit, the inertia is negligible thus the amplitude equation takes the form [amplitude Eq. (6)]

$$\gamma\partial_t A = \mu A - aA|A|^2 + \nabla_\perp^2 A + \delta\partial_{\eta\eta} \bar{A} + f(r)e^{i\theta}.$$

References

- [1] Pethick CJ, Smith H. Bose-Einstein condensation in dilute gases. New York: Cambridge University Press; 2008.
- [2] Tsuneto T. Superconductivity and superfluidity. New York: Cambridge University Press; 2005.
- [3] Tinkham M. Introduction to superconductivity. New York: McGraw-Hill; 1996.
- [4] Mühlbauer S, Binz B, Jonietz F, Pfleiderer C, Rosch A, Neubauer A, et al. Skyrmion lattice in a chiral magnet. Science 2009;323:915.
- [5] de Gennes PG, Prost J. The physics of liquid crystals. 2nd edn. Oxford Science Publications, Clarendon Press; 1993.
- [6] Berezinskii VL. Destruction of long-range order in one-dimensional and two-dimensional systems having a continuous symmetry group I. Classical systems. Sov Phys—JETP 1971;32:493.
- [7] Kosterlitz JM, Thouless DJ. Ordering, metastability and phase transitions in two-dimensional systems. J Phys: Condens Matter 1973;6:1181.
- [8] Pismen LM. Vortices in nonlinear fields. New York: Oxford Science; 1999.
- [9] Chandrasekhar S. Liquid crystals. Cambridge, UK: Cambridge University Press; 1992.
- [10] Rapini A. Umbilics: static properties and shear-induced displacements. J Phys 1973;34:629.

- [11] Barboza R, Sauma T, Bortolozzo U, Assanto G, Clerc MG, Residori S. Characterization of vortex pair interaction law and nonlinear mobility effects. *New J Phys* 2013;15:013028.
- [12] Kim M, Serra F. Tunable dynamic topological defect pattern formation in nematic liquid crystals. *Adv Opt Mater* 2020;8:1900991.
- [13] Sasaki Y, Jampani VSR, Tanaka C, Sakurai N, Sakane S, Le KV, et al. Large-scale self-organization of reconfigurable topological defect networks in nematic liquid crystals. *Nat Commun* 2016;7:13238.
- [14] Harkai S, Murray BS, Rosenblatt C, Kralj S. Electric field driven reconfigurable multistable topological defect patterns. *Phys Rev Res* 2020;2:013176.
- [15] Loussert C, Kushnir K, Brasselet E. Q-plates micro-arrays for parallel processing of the photon orbital angular momentum. *Appl Phys Lett* 2014;105:121108.
- [16] Salamon P, Éber N, Sasaki Y, Orihara H, Buka Á, Araoka F. Tunable optical vortices generated by self-assembled defect structures in nematics. *Phys Rev Appl* 2018;10:044008.
- [17] Pieranski P, Dubois-Violette E, Guyon E. Heat convection in liquid crystals heated from above. *Phys Rev Lett* 1973;30:736.
- [18] Clerc MG, Kowalczyk M, Zambra V. Topological transitions in an oscillatory driven liquid crystal cell. *Sci Rep* 2020;10:19324.
- [19] Calisto E, Clerc MG, Zambra V. Magnetic field-induced vortex triplet and vortex lattice in a liquid crystal cell. *Phys Rev Res* 2020;2: 042026(R).
- [20] Clerc MG, Ferre M, Gajardo-Pizarro R, Zambra V. Dancing vortices in a driven nematic liquid crystal cell: Theory and experiment. *Phys Rev E* 2022;106:L012201.
- [21] Fréedericksz V, Zolina V. Forces causing the orientation of an anisotropic liquid. *Trans Faraday Soc* 1927;29:919.
- [22] See Supplemental Material, video 1 shows experimental and numerical movies of the emergence of vortex lattices by nullcline entanglement. Video 2 shows an equilibrium vortex lattice.
- [23] Lifshitz E, Landau LD. On the theory of the dispersion of magnetic permeability in ferromagnetic bodies. *Phys Z Sowjet* 1935;8:135.
- [24] Barboza R, Bortolozzo U, Clerc MG, Residori S, Vidal-Henriquez E. Optical vortex induction via light-matter interaction in liquid-crystal media. *Adv Opt Photon* 2015;7:635.
- [25] Khoo IC, Lindquist RG, Michael RR, Mansfield RJ, LoPresti P. Dynamics of picosecond laser-induced density, temperature, and flow-reorientation effects in the mesophases of liquid crystals. *J Appl Phys* 1991;69:3853–9.
- [26] Eichler HJ, Macdonald R. Flow-alignment and inertial effects in picosecond laser-induced reorientation phenomena of nematic liquid crystals. *Phys Rev Lett* 1991;67:2666.
- [27] Silva AT, Dos Santos MAF, Lenzi EK, Evangelista LR, Zola RS. Modeling nematic liquid crystals: Analytical solution for the balance of torques equation with moment of inertia and surface viscosity. *Mol Cryst Liq Cryst* 2013;576.
- [28] Aranson IS, Kramer L. The world of the complex Ginzburg–Landau equation. *Rev Modern Phys* 2002;74:99.
- [29] Saupe A. On molecular structure and physical properties of thermotropic liquid crystals. *Mol Cryst Liq Cryst* 1969;7:59.
- [30] Belyaev VV. The viscosity of nematic liquid crystals. *Russ Chem Rev* 1989;58:917.
- [31] Migara LK, Song J-K. Standing wave-mediated molecular reorientation and spontaneous formation of tunable, concentric defect arrays in liquid crystal cells. *NPG Asia Mater* 2018;10:e459.
- [32] Panov VP, Yang J, Migara LK, Yoon HJ, Song JK. Rotation-time symmetry breaking in frustrated chiral nematic driven by a pulse-train waveform. *Phys Rev Lett* 2022;129:117801.